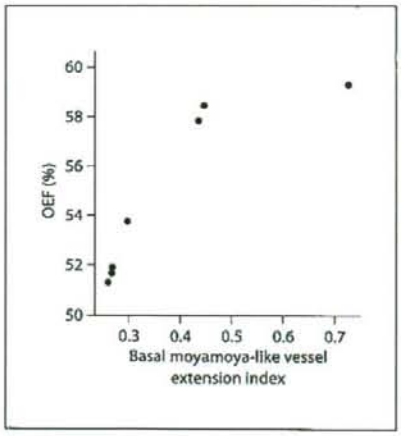

Fig. 3. The extent of the development of angiographic basal moyamoya-like vessels in the moyamoya syndrome group was evaluated by DSA. The ratio of the distance from the root to the top-end of the basal moyamoya-like vessels to the distance from the base of the skull (top of the sella turcica) to the top of the skull in the same plane was indicated as the basal moyamoya-like vessel extension index. Regional OEF was measured by positron emission tomography in the cortical MCA area.

Discussion

The hemodynamic and metabolic backgrounds of moyamoya syndrome associated with atherosclerosis have not yet been investigated. In the present study, we aimed to elucidate the hemodynamic and metabolic changes associated with moyamoya syndrome with atherosclerosis, and evaluated the hemodynamic and metabolic changes associated with the development of the moyamoya-like vascular abnormality associated with unilateral atherosclerotic steno-occlusive lesions of the ICA or MCA in the chronic phase. We demonstrated that the cerebral hemodynamic impairment was significantly more severe in patients with moyamoya syndrome than in those without moyamoya syndrome.

We demonstrated previously that among cases of moyamoya disease, the OEF was significantly higher in adult patients with extensively developed basal moyamoya vessels than in those with less extensive development of moyamoya vessels and normal controls [2]. According to a perfusion-weighted MRI study [3], the extent of development of moyamoya vessels in both childhood and adult moyamoya disease was correlated with the mean transit time, which has been shown to be an alternative index to the OEF [11]. In the present study, it was demonstrated that the presence and extent of development of the moyamoya-like vessels were also correlated with the severity of the cerebral hemodynamic impairment in the ipsilateral cortical MCA territory.

It has been shown that in moyamoya disease, the extent of development of the basal moyamoya vessels is negatively correlated with the extent of development of leptomeningeal collateral vessels from the PCA, and positively correlated with the severity of the stenotic lesions in the major arterial trunks [12]. In the present study, the degree of the total vascularity, excluding that of the moyamoya-like vessels, in the ipsilateral hemisphere was significantly worse in the moyamoya syndrome group than in the non-moyamoya-syndrome group. Both in moyamoya disease and in moyamoya syndrome, the basal moyamoya or moyamoya-like vessels, which are considered to be types of collateral vessels in moyamoya disease [5, 13], were found to have developed to complement the insufficient collateral networks in the ipsilateral cortical area.

The present study had some limitations. Firstly, the number of patients was so small that statistical reliability could not be ensured. Secondly, the normal controls enrolled in this study were younger than the patient group. In this study, however, we focused on comparisons between the patient groups, because there have been numerous comparative studies about cerebral hemodynamic and oxygen metabolism by PET between normal controls and patients with atherosclerotic steno-occlusive lesions. Thirdly, the ROI settings by the automated ROI analysis program FineSRT are sometimes inappropriate because of errors in normalization procedures, brain atrophy by aging, artifacts by gas masks or displacement of sinuses. In the present study, we visually checked all the ROI settings via the viewer window and eliminated apparently inappropriate ROI from the analysis. Fourthly, although we have suggested that cerebral hemodynamic compromise may be responsible for the development of moyamoya-like vessels, hereditary factors may also be involved in this angiogenesis because the incidence of moyamoya disease is comparatively higher in the Japanese [13] and Koreans [14], and markedly lower in Caucasians. Further studies are needed to elucidate the effects of racial differences and genetic factors on the development of moyamoya-like vessels.

Conclusion

The hemodynamic and metabolic backgrounds of moyamoya syndrome associated with atherosclerosis have not yet been investigated. The present study clarified that the development of the basal moyamoya-like vascular abnormality is an important sign of misery perfusion in the ipsilateral cortical MCA territory in patients with moyamoya syndrome associated with unilateral chronic atherosclerotic steno-occlusive lesions.

Acknowledgments

We thank Mr. Yukio Nakamura and the staff of the Department of Nuclear Medicine and the Cyclotron staff of Osaka University Hospital for their technical support in performing the studies. This study was partly supported by a grant from the Research Committee on Moyamoya Disease established by the Ministry of Health, Labor and Welfare of Japan.

References

1 Suzuki J, Takaku A: Cerebrovascular 'moyamoya' disease: disease showing abnormal net-like vessels in base of brain. Arch Neurol 1969;20:288–299.

2 Piao R, Oku N, Kitagawa K, Imaizumi M, Matsushita K, Yoshikawa T, Takasawa M, Osaki Y, Kimura Y, Kajimoto K, Hori M, Hatazawa J: Cerebral hemodynamics and metabolism in adult moyamoya disease: comparison of angiographic collateral circulation. Ann Nucl Med 2004;18:115–121.

3 Togao O, Mihara F, Yoshiura T, Tanaka A, Noguchi T, Kuwabara Y, Kaneko K, Matsushima T, Honda H: Cerebral hemodynamics in Moyamoya disease: correlation between perfusion-weighted MR imaging and cerebral angiography. AJNR Am J Neuroradiol 2006;27:391–397.

4 Adams HP Jr: Moya-Moya; in Bogousslavsky J, Caplan LR (eds): Uncommon Causes of Stroke. Cambridge, Cambridge University Press, 2001, pp 241–257.

5 Hinshaw DB Jr, Thompson JR, Hasso AN: Adult arteriosclerotic moyamoya. Radiology 1976;118:633–636.

6 Cerrato P, Grasso M, Lentini A, Destefanis E, Bosco G, Caprioli M, Bradac GB, Bergui M: Atherosclerotic adult Moya-Moya disease in a patient with hyperhomocysteinaemia. Neurol Sci 2007;28:45–47.

7 Beneficial effect of carotid endarterectomy in symptomatic patients with high-grade carotid stenosis. North American Symptomatic Carotid Endarterectomy Trial Collaborators. N Engl J Med 1991;325:445–453.

8 Frackowiak RS, Lenzi GL, Jones T, Heather JD: Quantitative measurement of regional cerebral blood flow and oxygen metabolism in man using ^{15}O and positron emission tomography: theory, procedure, and normal values. J Comput Assist Tomogr 1980;4:727–736.

9 Lammertsma AA, Jones T: Correction for the presence of intravascular oxygen-15 in the steady-state technique for measuring regional oxygen extraction ratio in the brain. 1. Description of the method. J Cereb Blood Flow Metab 1983;3:416–424.

10 Takeuchi R, Sengoku T, Matsumura K: Usefulness of fully automated constant ROI analysis software for the brain: 3DSRT and FineSRT. Radiat Med 2006;24:538–544.

11 Tanaka Y, Nariai T, Nagaoka T, Akimoto H, Ishiwata K, Ishii K, Matsushima Y, Ohno K: Quantitative evaluation of cerebral hemodynamics in patients with moyamoya disease by dynamic susceptibility contrast magnetic resonance imaging – comparison with positron emission tomography. J Cereb Blood Flow Metab 2006;26:291–300.

12 Yamada I, Himeno Y, Suzuki S, Matsushima Y: Posterior circulation in moyamoya disease: angiographic study. Radiology 1995; 197:239–246.

13 Fukui M, Kono S, Sueishi K, Ikezaki K: Moyamoya disease. Neuropathology 2000; 20(suppl):S61–S64.

14 Park J, Hwang YH, Baik SK, Kim YS, Park SH, Hamm IS: Angiographic examination of spontaneous putaminal hemorrhage. Cerebrovasc Dis 2007;24:434–438.

MRI-Based Correction for Partial-Volume Effect Improves Detectability of Intractable Epileptogenic Foci on ^{123}I-Iomazenil Brain SPECT Images

Hiroki Kato[1], Eku Shimosegawa[1], Naohiko Oku[2], Kazuo Kitagawa[3], Haruhiko Kishima[4], Youichi Saitoh[4], Amami Kato[5], Toshiki Yoshimine[4], and Jun Hatazawa[1]

[1]Department of Nuclear Medicine and Tracer Kinetics, Osaka University Graduate School of Medicine, Suita, Japan; [2]Department of Nuclear Medicine, Hyogo College of Medicine, Nishinomiya, Japan; [3]Department of Neurology, Osaka University Graduate School of Medicine, Suita, Japan; [4]Department of Neurosurgery, Osaka University Graduate School of Medicine, Suita, Japan; and [5]Department of Neurosurgery, Kinki University School of Medicine, Osaka-Sayama, Japan

^{123}I-Iomazenil brain SPECT has been used for the detection of epileptogenic foci, especially when surgical intervention is considered. Although epileptogenic foci exhibit a decrease in ^{123}I-iomazenil accumulation, normal cerebral cortices often exhibit similar findings because of thin cortical ribbons, gray matter atrophy, or pathologic brain structures. In the present study, we created ^{123}I-iomazenil SPECT images corrected for gray matter volume using MRI and tested whether the detectability of the epileptogenic foci improved. **Methods:** Seven patients (1 male patient and 6 female patients; mean age ± SD, 34 ± 17 y) with intractable epilepsy were surgically treated by resecting the cerebral cortex after surface electroencephalography. Histopathologic examination of the resected specimens and a good outcome after surgery indicated that the resected lesions were epileptogenic foci. These patients underwent ^{123}I-iomazenil SPECT and 3-dimensional T1-weighted MRI examinations before their operations. Each SPECT image was coregistered to the corresponding MR image, and its partial-volume effect (PVE) was corrected on a voxel-by-voxel basis with a smoothed gray matter distribution image. Four nuclear medicine physicians visually evaluated the ^{123}I-iomazenil SPECT images with and without the PVE correction. The SPECT count ratio of the suspected focus to the contralateral cerebral cortex was evaluated as an asymmetry index (%) based on the volume of interest. **Results:** The sensitivity, specificity, and accuracy of focus detection by visual assessment were higher after PVE correction (88%, 99%, and 98%, respectively) than before correction (50%, 92%, and 87%, respectively). The mean asymmetry index for the surgically resected lesions was significantly higher on the PVE-corrected SPECT images (22%) than on the PVE-uncorrected ones (16%) ($P = 0.006$). **Conclusion:** MRI-based PVE correction for ^{123}I-iomazenil brain SPECT improves the sensitivity and specificity of the detection of cortical epileptogenic foci in patients with intractable epilepsy.

Key Words: epilepsy; ^{123}I-iomazenil; SPECT; MRI; partial-volume effect

J Nucl Med 2008; 49:383–389
DOI: 10.2967/jnumed.107.046136

Iomazenil labeled with ^{123}I is a tracer that is specifically bound to central benzodiazepine receptors (*1*). Because epileptogenic foci exhibit a reduction in central benzodiazepine receptors (*2,3*), ^{123}I-iomazenil brain SPECT has been used to detect epileptic foci, especially when surgical intervention is considered (*3*). However, normal cerebral cortices often exhibit similar findings on ^{123}I-iomazenil SPECT because of thin cortical ribbons, gray matter atrophy, or pathologic brain structures. This limitation is caused by the partial-volume effect (PVE), which arises from the limited spatial resolution of the scanner. In small structures, the observed radioactivity concentration differs from the true concentration because of blurring of the counts out of the structure ("spill-out") and blurring of the counts into the structure from the surrounding radioactivity ("spill-in") (*4*).

In a previous study (*5*) examining patients with intractable mesial temporal lobe epilepsy arising from hippocampal sclerosis, the sensitivity of detecting pathologic hippocampi using ^{11}C-flumazenil PET was improved by PVE correction using MRI-based measurements of hippocampal volume. In the present study, we created ^{123}I-iomazenil SPECT images corrected for the whole-brain gray matter volume based on MRI measurements in patients with intractable partial epilepsy and tested whether the detectability of cortical epileptogenic foci improved.

MATERIALS AND METHODS

Patients

Seven patients with intractable epilepsy (1 male patient and 6 female patients; mean age ± SD, 34 ± 17 y) who met the following criteria were studied: no morphologic brain lesions other than small

Received Aug. 7, 2007; revision accepted Nov. 20, 2007.
For correspondence or reprints contact: Jun Hatazawa, MD, PhD, Osaka University Graduate School of Medicine, 2-2 Yamadaoka, Suita, 565-0871, Japan.
E-mail: hatazawa@tracer.med.osaka-u.ac.jp

cystic lesions or suspected unilateral hippocampal atrophy (hippocampal sclerosis) visible on routine conventional MR images, surgical removal and histopathologic examination of suspected epileptogenic foci, improvement of patients' symptoms after surgery, and performance of ^{123}I-iomazenil brain SPECT and 3-dimensional (3D) T1-weighted MRI studies before operation.

The patients' clinical information is summarized in Table 1. All patients had complex partial seizures with or without generalization and were being treated with anticonvulsants. The Wada test, verbal magnetoencephalogram, or Edinburgh test was performed to determine the lateralization of verbal function or memory. All patients underwent surface electroencephalography or magnetoencephalography to identify the location and extent of the epileptogenic foci. All specimens resected during the operations were histopathologically investigated (Table 2). The histologic findings in 5 of 7 patients were nonspecific gliosis or neurodegeneration, and 1 patient (patient 3) was suspected of having astrocytoma. The outcome after surgery was evaluated on the basis of Engel's classification. The average follow-up period after surgery was 14 mo (range, 9–18 mo). Five patients were classified as Engel's classification I, and the remaining patients as Engel's classification III.

SPECT

In each subject, 167 MBq of ^{123}I-iomazenil were intravenously administered. Three hours after the injection, SPECT images were acquired while the subject rested supine on the scanning bed with eyes closed in a quiet room. SPECT was performed using a 4-head γ-camera (*6*) (Gamma View SPECT 2000H; Hitachi Medical Corp.) with a low-energy middle-resolution thin-section parallel-hole collimator. After the patient's head had been fixed on the headrest, the orbitomeatal line was detected using a laser-assisted device equipped with the γ-camera. The acquisition protocol was 20 s per step, with 64 collections over 360°, and the data were recorded in a 64 × 64 matrix. The raw SPECT data were transferred to a nuclear medicine computer (HARP 3; Hitachi Medical Corp.). The projection data were prefiltered using a Butterworth filter (cutoff frequency, 0.20 cycles per pixel; order, 10) and reconstructed into transaxial sections of 4.0-mm thickness in planes parallel to the orbitomeatal line. Attenuation correction was performed using Chang's method (*7*) with an optimized effective attenuation coefficient of 0.08 cm^{-1}.

PVE Correction

PVE was corrected using 3D T1-weighted MRI and a personal computer (Dell Dimension 8300; Dell Inc.) running Windows XP (Microsoft Corp.), as described in Figure 1. Thin-slice sagittal 3D T1-weighted MR images were produced using 3 types of MRI scanners: a Signa Excite 3.0 T, a Signa Excite HD 1.5 T (GE Yokogawa Medical Systems Ltd.), and a Magnetom Vision Plus 1.5 T (Siemens AG). In each case, a spoiled gradient echo sequence was used (echo time/repetition time: 1.928/8.632 ms, 1.820/8.552 ms, and 4.700/9.000 ms for the respective scanners; flip angle: 18, 18, and 12, respectively; acquisition matrix: all 256 × 256; slice thickness: all 1.4 mm). The acquired sagittal images were reformatted to axial images with a thickness of 1.4 mm.

The T1-weighted MR images were first segmented into gray matter, white matter, cerebrospinal fluid, or other compartments (skull and extracranial structures) using SPM5 (Wellcome Department of Imaging Neuroscience). This procedure yielded a Bayesian probability map for each tissue class based on a priori MRI information with an inhomogeneity correction for the magnetic field (*8*). Voxels were assigned into 3 tissue classes (gray matter, white matter, and cerebrospinal fluid) according to the maximum probability encountered for each voxel across the 3 datasets. These 3 tissue classes were subsequently put into binary form (given a value of 0 for absence of tissue or 1 for presence of tissue) (*9*).

The point-spreading function of the reconstructed SPECT images acquired with the low-energy middle-resolution thin-section parallel-hole collimator was assessed using a ^{123}I 1-mm-diameter line source in air, according to a previously described methodology (*6*). The binary maps for the gray matter were convoluted with a 3D gaussian function with a full width at half maximum of 12 × 12 × 12 mm, which was assumed to be the same as the point-spreading function of the reconstructed SPECT image, as described in previous studies (*10,11*). The resulting image was subsequently referred to as the smoothed gray matter map.

The ^{123}I-iomazenil SPECT images were coregistered to the smoothed gray matter maps using FMRIB's Linear Image Registration Tool (FLIRT) (*12*). In this procedure, the ^{123}I-iomazenil SPECT images were simultaneously reformatted to a matrix of the same size (256 × 256 × 256) as the referenced smoothed gray matter maps.

A binary volume image was created from the smoothed gray matter map as a mask image for the gray matter. The threshold for determining

TABLE 1
Characteristics of Subjects

Patient no.	Age (y)	Sex	Onset (y)	Duration (y)	Seizures/mo	Interval* (d)	Diagnosis	Anticonvulsants	MRI	Language dominancy
1	24	F	14	10	120	4	LTLE	CBZ, CLB	NP	L (Wada test)
2	65	F	43	22	30	2	MTLE	PHT	NP	Bilateral (Wada test)
3	44	F	40	4	30	2	LTLE	None	Small cyst in R ATL	Bilateral (Wada test)
4	14	F	3	11	5	10	MTLE	VPA, CBZ, PHT	NP	L (MEG study)
5	30	F	8	22	10	7	MTLE	CBZ, CLB, CZP	R HS	L (Wada test)
6	28	F	19	9	5	3	MTLE	VPA	L HS	L (Edinburgh test)
7	31	M	9	22	8	2	LTLE	CBZ, CLB, CZP	NP	R (Wada test)

*Between last seizure and SPECT study.

LTLE = lateral temporal lobe epilepsy; CBZ = carbamazepine; CLB = clobazam; NP = not performed; MTLE = mesial temporal lobe epilepsy; PHT = phenytoin; ATL = anterior temporal lobe; VPA = sodium valproate; MEG = magnetoencephalogram; CZP = clonazepam; HS = hippocampal sclerosis.

TABLE 2
Operations and Prognosis

Patient no.	Resected lesions	Histology	Prognosis*	Follow-up (mo)
1	L superior temporal gyrus, middle temporal gyrus (corticectomy/multiple subpial transection)	Gliosis	IIc	18
2	L hippocampus (multiple subpial transection), L superior temporal gyrus (corticectomy)	Gliosis	Ib	17
3	R anterior temporal lobe (tailored lobectomy), R hippocampus (hippocampectomy)	Astrocytoma	Ia–Ib	16
4	R hippocampus (hippocampectomy), temporal lobe (tailored corticectomy)	Gliosis, degeneration	Id	14
5	R hippocampus (hippocampectomy), anterior temporal lobe (tailored lobectomy), superior temporal gyrus (corticectomy)	Satellitosis	Ia	14
6	L hippocampus (hippocampectomy), amygdaloid (amygdaloidectomy)	Neurodegeneration	Ia	9
7	L posterior central gyrus, angular gyrus (selective corticectomy/multiple subpial transection)	Unknown	IIIa	9

*Engel's classification. Class I: free of disabling seizures (completely seizure-free since surgery [Ia], nondisabling simple partial seizures [Ib], some disabling seizures but free of disabling seizures for at least 2 y ["running down"] [Ic], generalized convulsion with antiepileptic drug withdrawal only [Id]). Class II: rare disabling seizures (rare disabling seizures since surgery [<3/y] [IIa], more than rare disabling seizures initially but only rare seizures for at least 2 y [IIb], nocturnal seizures only [IIc]). Class III: worthwhile improvement (significant reduction in seizure frequency [>75% reduction] [IIIa], prolonged seizure-free intervals amounting to greater than half the follow-up period of at least 2 y [IIIb]). Class IV: no worthwhile improvement (insignificant reduction, no change, or increase in seizure frequency).

the boundary of the binary volume image was set at 35% (an empirically determined value) of the maximum, which was the same as the threshold value used in a previous study (*10*). This mask image for the gray matter was then applied to the coregistered ^{123}I-iomazenil SPECT image. The masked ^{123}I-iomazenil SPECT image was then divided using the smoothed gray matter map on a pixel-by-pixel basis (Fig. 1).

Visual Assessment

Four experienced nuclear medicine physicians visually assessed the coronal images. The physicians were unaware of the patients' clinical information to avoid biases caused by differences in the amount of information available for each of the patients. The physicians visually evaluated the coronal ^{123}I-iomazenil SPECT images with and without PVE correction, presented in a random order, and noted the areas of epileptogenic foci, where the tracer uptake was reduced when compared with the corresponding contralateral regions. Decisions on the foci were made by joint agreement during a conference of the 4 physicians.

Patients without epileptogenic foci were excluded from the present study. Therefore, the sensitivity and specificity of focus

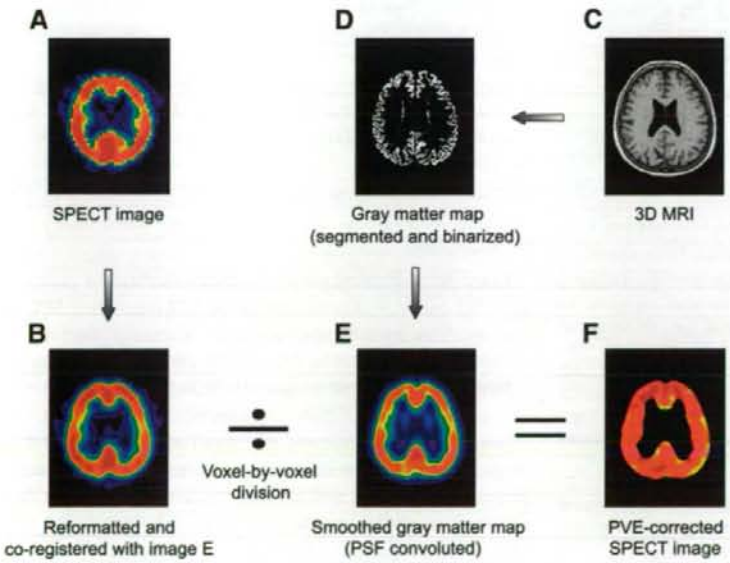

FIGURE 1. (A) ^{123}I-Iomazenil SPECT image. (B) Automatic coregistration of ^{123}I-iomazenil SPECT image with MR image via smoothed gray matter maps. Maps were simultaneously reformatted to matrix that was same size as referenced smoothed gray matter map. (C) 3D MR image obtained before operation. (D) MR image segmented into Bayesian probability map showing 3 tissue classes. Gray matter probability map was subsequently put into binary form (0 for absence of tissue, 1 for presence of tissue). (E) Binary map for gray matter convoluted with point-spreading function (PSF), which was assumed to be same as point-spreading function of SPECT scanner. (F) Smoothed gray matter map masked with threshold set to 35% of maximum voxel value. Coregistered ^{123}I-iomazenil SPECT image was divided using masked smoothed gray matter map on voxel-by-voxel basis.

detection were determined on a region-by-region basis. We divided the whole cerebrum into 18 bilateral blocks, as shown in Figure 2. We then assigned a binary value of positive or negative to each block, based on the visual assessment (i.e., positive for a focus, negative for no focus). We assumed that the resected lesions corresponded to the true epileptogenic foci and that unresected regions corresponded to the intact brain, because follow-up of surgical outcomes of the patients was good. Then, a true-positive result was defined as a positive result of visual assessment in a resected brain region, a true-negative result was defined as a negative result of visual assessment in an unresected brain region, a false-positive result was defined as a positive result of visual assessment in an unresected brain region, and a false-negative result was defined as a negative result of visual assessment in a resected brain region. The sensitivity, specificity, and accuracy of uncorrected or PVE-corrected SPECT images were calculated as follows:

$$\text{sensitivity} = \text{number of true-positive blocks}/\text{number of resected blocks},$$

$$\text{specificity} = \text{number of true-negative blocks}/\text{number of unresected blocks},$$

$$\text{accuracy} = (\text{number of true-positive blocks} + \text{number of true-negative blocks})/\text{number of total blocks}.$$

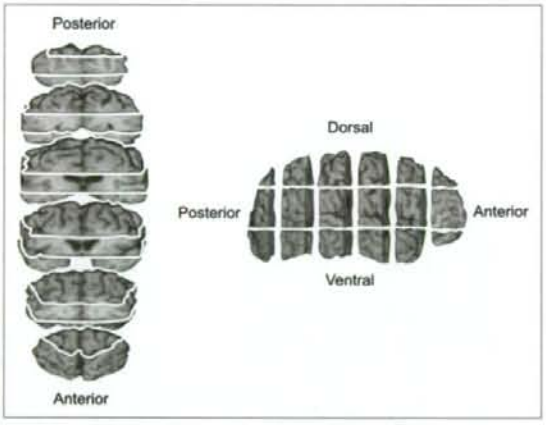

FIGURE 2. Whole cerebrum was divided into 18 bilateral blocks. A binary value of positive or negative was assigned to each block on the basis of visual assessment (i.e., positive for focus, negative for no focus). In this study, we assumed that resected lesions corresponded to true epileptogenic foci and unresected regions corresponded to intact brain because of good follow-up outcomes of patients after operations. Then, result of evaluation of each block was defined as follows. true-positive: positive result of visual assessment in resected brain region; true-negative: negative result of visual assessment in unresected brain region; false-positive: positive result of visual assessment in unresected brain region; false-negative: negative result of visual assessment in resected brain region.

Quantitative Assessment

First, the volume of interest (VOI) was established so as to include each resected lesion in reference to an MR image obtained after the operation (Fig. 3). If the VOI included a medial temporal lesion, it was divided into a medial temporal and a lateral part. Second, another VOI was made so as to contain each visually detected false-positive area on the uncorrected or PVE-corrected SPECT images that were coregistered with the MR images. For each of these VOIs, the corresponding contralateral VOI was also made in reference to the SPECT and MR images. The VOI counts of the uncorrected or the PVE-corrected SPECT images coregistered with the MR images were measured to evaluate quantitatively the sensitivity or specificity of the images of the epileptogenic foci. The asymmetry index (AI) for the ^{123}I-iomazenil SPECT count of the ipsilateral VOI A, C_A, and that of the contralateral VOI B, C_B, was calculated as follows:

$$AI = |C_A - C_B| \times 200/(C_A + C_B). \qquad \text{Eq. 1}$$

RESULTS

The sensitivity, specificity, and accuracy of focus detection by visual assessment were higher after PVE correction (88%, 99%, and 98%, respectively) than before correction (50%, 92%, and 87%, respectively). The AI values for the resected lesions are summarized in Table 3. The mean AI was significantly higher on the PVE-corrected SPECT images than on the uncorrected ones for the whole resected lesions (22%, 16%, $P = 0.006$), lateral parts of the resected lesions (20%, 12%, $P = 0.006$), and medial temporal parts of the resected lesions (25%, 20%, $P = 0.029$). In patients 2 and 7, true foci were not detected on the uncorrected SPECT images. In Table 4, the location, visual assessment, and AI for the false-positive regions are listed. The mean AI for the false-positive regions was significantly larger on the uncorrected images (12%) than on the PVE-corrected ones (4.8%) ($P < 0.001$).

The uncorrected and PVE-corrected SPECT images of typical patients are shown in Figure 4. A lateralized decrease in the counts was found on the PVE-corrected images in the areas corresponding to the resected lesions, although no laterality was seen on the uncorrected images (Fig. 4A). Conversely, a lateralized decrease in the counts was seen in the intact areas on the uncorrected images, whereas no laterality was found on the PVE-corrected images (Fig. 4B).

DISCUSSION

In the present study, we introduced a method for performing MRI-based PVE corrections on ^{123}I-iomazenil SPECT images. This method improved the accuracy with which epileptogenic foci can be detected in the cerebral cortices.

Inhibitory neural transmission is thought to be disturbed at epileptic foci (*13*). This hypothesis is supported by in vivo flumazenil PET (*14,15*) and iomazenil SPECT (*2,3*) studies. Previous studies have indicated a disproportion between the gray matter volume and the benzodiazepine receptor density in some epileptogenic foci (*3,16,17*). In patients with hippocampal sclerosis, changes in benzodiazepine receptor

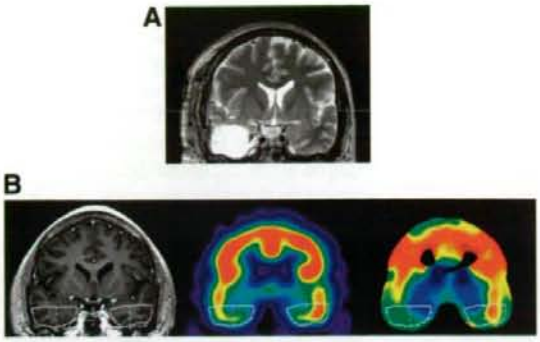

FIGURE 3. (A) MR image obtained after operation. (B) VOIs for resected brain lesions were established on 3D MR image (left) so as to include each resected lesion in reference to MR image obtained after operation. Corresponding contralateral VOIs were also established on same MR image. If VOI included medial temporal area, it was divided into lateral temporal part and medial temporal part (dashed line). Each VOI was applied to uncorrected (middle) and PVE-corrected (right) SPECT images coregistered to 3D MR image.

binding were detected in the hippocampus and the extrahippocampal neocortices, which appeared normal on MRI (*18*). Thus, identifying the location of epileptogenic foci and evaluating the extent of the area to be resected may be impossible using MRI alone. In the present study, a considerable number of true-positive lesions in the cerebral cortices appeared normal during the MRI study.

The nonspecific binding of iomazenil has been shown to account for a small proportion of all bound molecules (1%–3%) (*19*). According to an ex vivo study of nonhuman primates, iomazenil showed a predominantly high accumulation in the gray matter, with ratios of greater than 30:1 for gray matter to white matter (*20*). Thus, the distribution of iomazenil accumulation in the cerebrum is markedly influenced by the local volume of gray matter when a SPECT scanner with a limited spatial resolution is used. Nonpathologic laterality or an asymmetric distribution of gray matter volume on a certain slice may increase the risk of a false-positive result in side-by-side comparisons of iomazenil images.

The accurate determination of actual radiotracer concentrations in human gray matter in vivo is possible using MRI-based PVE corrections (*21,22*). In ethylcysteinate dimer SPECT, PVE correction made the regional cerebral blood flow distribution more homogeneous throughout the brain, with less intersubject variation than in the original distribution. Using this method for brain perfusion SPECT determines regional cerebral blood flow more accurately, even in healthy volunteers (*10*). As for ^{15}O-H_2O PET, PVE correction made it possible to estimate the regional cerebral blood flow accurately despite cortical atrophy both in Alzheimer's disease (*23*) and in normal aging (*24*). In ^{18}F-FCWAY (^{18}F-*trans*-4-fluoro-*N*-2-[4-(2-methoxyphenyl)piperazin-1-yl]ethyl-*N*-(2-pyridyl)cyclohexanecarboxamide) PET for the detection of foci in TLE patients, MRI-based PVE correction effectively eliminated artifacts related to PVE that were influenced by the local geometry of the gray matter and was useful for the extraction of pathologic serotonin 1A binding reduction (*25*).

The MRI-based PVE correction method used in the present study is similar to that used in previous studies (*5,10,23,26*). In this study, PVE was corrected for gray matter and other components (2-compartment method), although the PVE correction was performed for gray matter, white matter, and other brain structures (3-compartment method) in most of the previous studies. According to a previous validation study (*21*), the 2-compartment method is less sensitive to errors resulting from resolution mismatch between MRI and SPECT, misregistration, and missegmentation. Meanwhile, the 3-compartment method is capable of greater accuracy for absolute quantitative measures. The accumulation of ^{123}I-iomazenil in white matter is known to be markedly small; consequently, the spill-in of counts from the surrounding white matter to the gray matter voxels is negligible. For this application, the 2-compartment method is more suitable because the decrease in accuracy is small and the tolerance to errors in image processing is greater with the 2-compartment method than with the 3-compartment one.

TABLE 3
AI for VOI Counts in Resected Lesions

Patient no.	Resected lesions	Total resected lesions (AI [%])		Lateral part of lesions (AI [%])		Medial temporal part of lesions (AI [%])	
		Uncorrected	PVE-corrected	Uncorrected	PVE-corrected	Uncorrected	PVE-corrected
1	STG, MTG	2.2	10.8	2.2	10.8	—	—
2	ATL, MTL	7.4	13.6	5.6	13.0	−0.2	10.8
3	ATL, MTL	21.7	34.4	21.3	34.2	9.6	15.3
4	ITG, MTL	29.5	38.7	24.7	34.5	39.4	46.4
5	ATL, MTL	12.2	14.6	10.0	13.2	21.1	22.5
6	MTL	27.8	30.6	—	—	27.8	30.6
7	IPL	9.1	11.6	9.1	11.6	—	—

STG = superior temporal gyrus; MTG = middle temporal gyrus; ATL = anterior temporal lobe; MTL = mesial temporal lobe; ITG = inferior temporal gyrus; IPL = inferior parietal lobule.

TABLE 4
AI for VOI in False-Positive Areas

Patient no.	Location	Uncorrected		PVE-corrected	
		Visual assessment	AI (%)	Visual assessment	AI (%)
1	ATL	Positive	15.0	Positive	13.1
2	MTL-WM*	Positive	10.7	Negative	2.1
	SPL	Positive	10.3	Negative	4.1
3	OG	Positive	11.1	Negative	7.2
	IPL	Positive	14.6	Negative	1.4
	SPL	Positive	10.1	Negative	4.6
5	PHG	Positive	12.0	Negative	1.2
6	ATL	Positive	13.6	Negative	7.3
7	SPL	Positive	11.6	Negative	2.1
	MTL	Positive	11.9	Negative	4.7

*Contralateral to true focus.

ATL = anterior temporal lobe; MTL-WM = mesial temporal lobe white matter; SPL = superior parietal lobule; OG = orbital gyri; IPL = inferior parietal lobule; PHG = parahippocampal gyrus; MTL = mesial temporal lobe.

In this study, an increase in the AI of the resected lesions was shown after PVE correction in both the lateral part and medial temporal part of the resected lesions. This finding implies an increase in the volume of the gray matter or decrease in the volume of the adjacent white matter in the lesion areas, compared with that in the corresponding contralateral normal areas. In the previous study (*27*), an increase in the regional gray matter concentration in malformations of cortical development in patients with focal cortical dysplasia was detected by voxel-based morphometry. In addition, the local increase of the gray matter volume has been reported to coincide with that of the white matter volume, as detected by voxel-based morphometry, around pathologic sclerotic medial temporal lesions in cases of temporal lobe epilepsy (*28*). This phenomenon may, however, be controversial, and further detailed investigation is needed of the changes in the AI in pathologic medial temporal lesions associated with PVE correction.

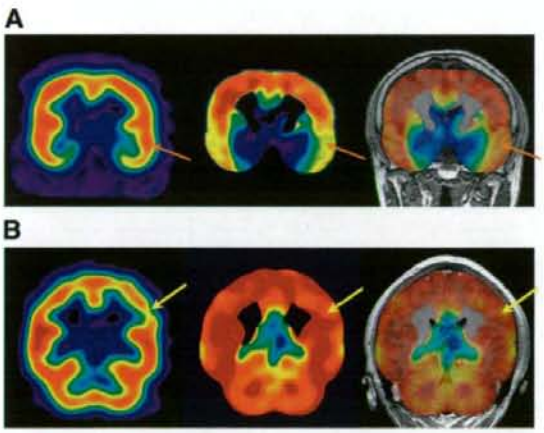

FIGURE 4. Typical SPECT images of 2 patients are shown. In each case, uncorrected SPECT image is on left, PVE-corrected SPECT image in middle, and PVE-corrected SPECT image coregistered to MR image on right. (A) Although no laterality could be found on uncorrected images, localized decrease in count on PVE-corrected images is distinct in areas corresponding to resected lesions. (B) No laterality was found on PVE-corrected images; unilateral decreased count, however, was found in intact areas on uncorrected images. Arrows indicate the true focus (red) or the false-positive region (yellow).

The present study had some limitations. First, the number of patients was too small to ensure statistical reliability. Second, some of the patients were taking anticonvulsants (e.g., clobazam) at the time of their ^{123}I-iomazenil SPECT examination, even though such drugs may influence iomazenil binding to a certain extent. Previous reports, however, have suggested that the extent of this influence is small (*3,29*). Thus, as far as intrasubject comparisons using the AI are concerned, the influence of anticonvulsants was thought to be negligible. Additionally, the temporary withdrawal of anticonvulsants solely for the purpose of SPECT can be harmful or impractical. From this viewpoint, our findings suggest that PVE corrections for ^{123}I-iomazenil SPECT remain effective even when the patient is taking anticonvulsants. Third, the brain structure images were obtained using 3 different types of MRI scanners. However, this protocol was not problematic in the present study because interscanner comparisons were not included in the analysis. Fourth, white matter activity was masked and eliminated during the process of PVE correction, although some cases of refractory focal epilepsy with heterotopia caused by neuronal migration disturbances have been reported to show a high flumazenil uptake in periventricular white matter (*30*). Because the evaluation of abnormal ^{123}I-iomazenil activity in white matter is quite difficult because of the higher activity spill-out from the adjacent gray matter, further study to solve this problem is needed. Fifth, the resolution of the present scanner was around 11 mm, although the current state-of-the-art SPECT scanner has a resolution of around 4–5 mm at full width at half maximum. We consider that the PVE correction in these scanners is effective to detect small cortical foci of epilepsy. Finally, we assumed that the unresected brain tissues were normal. Because this assumption cannot be proved, the accuracy of the true-negative and false-positive categorizations is limited.

CONCLUSION

PVE correction for ^{123}I-iomazenil brain SPECT images using the MRI-based gray matter volume improved the sensitivity and specificity at which cortical epileptogenic foci could be detected in patients with intractable epilepsy.

ACKNOWLEDGMENTS

We thank the staffs of the Department of Pathology, Osaka University Graduate School of Medicine, for their help with the histology; Dr. Yasuyuki Kimura, Dr. Katsufumi Kajimoto,

and Dr. Makiko Tanaka for their contribution to the SPECT data acquisition; and Yukio Nakamura and the staff of the Department of Nuclear Medicine and the cyclotron staff of Osaka University Hospital for their technical support in performing this study. This study was supported in part by a grant for molecular imaging project from the Japan Science Technology Agency.

REFERENCES

1. Beer HF, Blauenstein PA, Hasler PH, et al. In vitro and in vivo evaluation of iodine-123-Ro 16-0154: a new imaging agent for SPECT investigations of benzodiazepine receptors. *J Nucl Med.* 1990;31:1007–1014.
2. Morimoto K, Watanabe T, Ninomiya T, et al. Quantitative evaluation of central-type benzodiazepine receptors with [^{125}I]iomazenil in experimental epileptogenesis: II. The rat cortical dysplasia model. *Epilepsy Res.* 2004;61: 113–118.
3. Sata Y, Matsuda K, Mihara T, Aihara M, Yagi K, Yonekura Y. Quantitative analysis of benzodiazepine receptor in temporal lobe epilepsy: [^{123}I]iomazenil autoradiographic study of surgically resected specimens. *Epilepsia.* 2002;43: 1039–1048.
4. Hoffman EJ, Huang SC, Phelps ME. Quantitation in positron emission computed tomography: 1. Effect of object size. *J Comput Assist Tomogr.* 1979;3: 299–308.
5. Koepp MJ, Richardson MP, Labbe C, et al. ^{11}C-Flumazenil PET, volumetric MRI, and quantitative pathology in mesial temporal lobe epilepsy. *Neurology.* 1997;49:764–773.
6. Kimura K, Hashikawa K, Etani H, et al. A new apparatus for brain imaging: four-head rotating gamma camera single-photon emission computed tomograph. *J Nucl Med.* 1990;31:603–609.
7. Chang LT. A method for attenuation correction in radionuclide computed tomography. *IEEE Trans Nucl Sci.* 1978;25:638–643.
8. Ashburner J, Friston KJ. Voxel-based morphometry: the methods. *Neuroimage.* 2000;11:805–821.
9. Bencherif B, Stumpf MJ, Links JM, Frost JJ. Application of MRI-based partial-volume correction to the analysis of PET images of mu-opioid receptors using statistical parametric mapping. *J Nucl Med.* 2004;45:402–408.
10. Matsuda H, Ohnishi T, Asada T, et al. Correction for partial-volume effects on brain perfusion SPECT in healthy men. *J Nucl Med.* 2003;44:1243–1252.
11. Ibanez V, Pietrini P, Alexander GE, et al. Regional glucose metabolic abnormalities are not the result of atrophy in Alzheimer's disease. *Neurology.* 1998;50: 1585–1593.
12. Jenkinson M, Smith S. A global optimisation method for robust affine registration of brain images. *Med Image Anal.* 2001;5:143–156.
13. Savic I, Persson A, Roland P, Pauli S, Sedvall G, Widen L. In-vivo demonstration of reduced benzodiazepine receptor binding in human epileptic foci. *Lancet.* 1988;2:863–866.
14. Arnold S, Berthele A, Drzezga A, et al. Reduction of benzodiazepine receptor binding is related to the seizure onset zone in extratemporal focal cortical dysplasia. *Epilepsia.* 2000;41:818–824.
15. Juhasz C, Chugani DC, Muzik O, et al. Relationship of flumazenil and glucose PET abnormalities to neocortical epilepsy surgery outcome. *Neurology.* 2001;56:1650–1658.
16. Lamusuo S, Pitkanen A, Jutila L, et al. [^{11}C]Flumazenil binding in the medial temporal lobe in patients with temporal lobe epilepsy: correlation with hippocampal MR volumetry, T2 relaxometry, and neuropathology. *Neurology.* 2000; 54:2252–2260.
17. Hammers A, Koepp MJ, Richardson MP, et al. Central benzodiazepine receptors in malformations of cortical development: a quantitative study. *Brain.* 2001;124: 1555–1565.
18. Hammers A, Koepp MJ, Labbe C, et al. Neocortical abnormalities of [^{11}C]-flumazenil PET in mesial temporal lobe epilepsy. *Neurology.* 2001;56:897–906.
19. Videbaek C, Friberg L, Holm S, et al. Benzodiazepine receptor equilibrium constants for flumazenil and midazolam determined in humans with the single photon emission computer tomography tracer [^{123}I]iomazenil. *Eur J Pharmacol.* 1993;249:43–51.
20. Sybirska E, al-Tikriti M, Zoghbi SS, Baldwin RM, Johnson EW, Innis RB. SPECT imaging of the benzodiazepine receptor: autoradiographic comparison of receptor density and radioligand distribution. *Synapse.* 1992;12:119–128.
21. Meltzer CC, Kinahan PE, Greer PJ, et al. Comparative evaluation of MR-based partial-volume correction schemes for PET. *J Nucl Med.* 1999;40:2053–2065.
22. Muller-Gartner HW, Links JM, Prince JL, et al. Measurement of radiotracer concentration in brain gray matter using positron emission tomography: MRI-based correction for partial volume effects. *J Cereb Blood Flow Metab.* 1992;12: 571–583.
23. Meltzer CC, Leal JP, Mayberg HS, Wagner HN Jr, Frost JJ. Correction of PET data for partial volume effects in human cerebral cortex by MR imaging. *J Comput Assist Tomogr.* 1990;14:561–570.
24. Meltzer CC, Cantwell MN, Greer PJ, et al. Does cerebral blood flow decline in healthy aging? A PET study with partial-volume correction. *J Nucl Med.* 2000; 41:1842–1848.
25. Giovacchini G, Toczek MT, Bonwetsch R, et al. 5-HT 1A receptors are reduced in temporal lobe epilepsy after partial-volume correction. *J Nucl Med.* 2005;46: 1128–1135.
26. Koepp MJ, Woermann FG. Imaging structure and function in refractory focal epilepsy. *Lancet Neurol.* 2005;4:42–53.
27. Bonilha L, Montenegro MA, Rorden C, et al. Voxel-based morphometry reveals excess gray matter concentration in patients with focal cortical dysplasia. *Epilepsia.* 2006;47:908–915.
28. Bernasconi N, Duchesne S, Janke A, Lerch J, Collins DL, Bernasconi A. Whole-brain voxel-based statistical analysis of gray matter and white matter in temporal lobe epilepsy. *Neuroimage.* 2004;23:717–723.
29. Duncan S, Gillen GJ, Brodie MJ. Lack of effect of concomitant clobazam on interictal ^{123}I-iomazenil SPECT. *Epilepsy Res.* 1993;15:61–66.
30. Hammers A, Koepp MJ, Richardson MP, Hurlemann R, Brooks DJ, Duncan JS. Grey and white matter flumazenil binding in neocortical epilepsy with normal MRI: a PET study of 44 patients. *Brain.* 2003;126:1300–1318.

映像情報
Medical
A monthly Journal of Medical Imaging and Information

別刷

産業開発機構株式会社

●特集1●

CT技術のブレイクスルー

高解像度定量ピンホールSPECTイメージング ー小動物から臨床へー

奈良先端科学技術大学院大学 情報科学研究科[*1]／国立循環器病センター研究所 先進医工学センター 放射線医学部[*2]／筑波大学大学院 システム情報工学研究科[*3]

銭谷 勉[*1, 2]／渡部浩司[*2]／工藤博幸[*3]／飯田秀博[*2]

はじめに

創薬や新規治療法の評価を目的とした前臨床研究において、ラットやマウスなどの小動物モデルを利用したin vivoイメージングは必要不可欠である。さらに近年の分子イメージング分野の発展に伴い、小動物専用イメージング装置がさかんに開発、製品化されている。その中でもPET（Positron Emission Tomography）やSPECT（Single Photon Emission Computed Tomography）といった放射性同位元素を用いる核医学的検査手法は高い感度を有し、トレーサの集積に対して正確に比例した信号強度を提示するため、病態生理や病態生化学的な変化を定量的に評価することができることから、重要な役割を担っている。

臨床用SPECT装置の解像度は10mm程度であり、小動物の撮像には不十分である。ピンホールコリメータを利用すると小視野領域の像が拡大され、1mm以下の高解像度で小動物のイメージングが可能となる[1]。このため、現在実用化されている小動物用SPECT装置は、ほとんどピンホールコリメータを採用している[2]。ピンホールコリメータで撮像した場合、体軸方向の画像歪とデータ欠損（トランケーション）という2つの定量性を劣化させる問題がある。われわれはこれらの問題に対して、2軸収集法およびトランケーションを許す撮像・画像再構成法を開発した。

本稿では、ピンホールSPECTによる高解像度イメージング技術を簡単に述べた上で、ピンホールSPECTにおいて定量画像を得るためにわれわれが開発した、画像歪とトランケーションの問題を改善するための撮像・画像再構成技術を概説する。また、これらの技術を応用した小動物SPECT装置についても述べたいと思う。

最近われわれは、ピンホールSPECTのヒトのような大きな被写体を対象とする局所高解像度定量イメージングへの利用を考えている。このためのトランケーションを許す画像再構成法に関しても、最後に述べる。

ピンホールコリメータによる高解像度SPECT

SPECT装置は、原理的に放射性同位元素から放出されるガンマ線の飛来方向を特定するためのコリメータを必要とする。臨床用のSPECT装置では、一般的にパラレルホールコリメータが用いられており、解像度は10mm程度である。小動物イメージングでは対象臓器も小さいため、それに伴って高解像度が要求される。ピンホールコリメータは撮像対象がコリメータに近いほど像をより拡大できるため、空間解像度および感度を高くできる（図1）。1mm以下の解像度も比較的容易に実現できるため、小動物のイメージングに適している。

ピンホールSPECTにおける画像歪の改善

ピンホールコリメータを用いたSPECT装置では、原理上3次元のデータ収集を行っているが、コーンビーム型CTの3次元画像再構成法が必要となる。従来のピンホールSPECTでは、単一の円軌道で投影データを収集し、解析的なFiltered Back-Projection（FBP）法によって画像再構成していた。この画像再構成法によると、図2（上）のように再構成された画像は体軸方向に歪み、視野内の解像度が不均一となるため定量評価が困難であり、研究の域を脱しなかった。FBP法に代えてOSEM（Ordered Subsets Expectation Maximization）などの統計学に基づいた逐次近似画像再構成法を適用することで、画像の中央付近では歪みが大幅に改善された[3]。しかし、視野の周辺では依然として解像度の劣化は残っている。

われわれは、この原因を投影データの不完全性に起因するものと仮説を立て、Tuyが導出したコーンビームCTで、3次元画像再構成に必要な完全データを収集するための条件「被写体と交わるすべての平面が焦点（ピンホール）軌道と交わる」[4]を満たすように撮像軌道を図2（下）のような複数回転軸軌道とし、

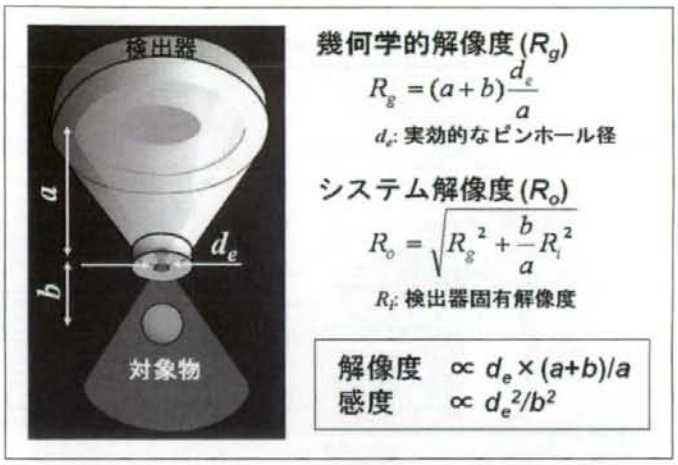

図1　ピンホールSPECTによる拡大撮像
撮像対象をコリメータに近づけるほど解像度や感度が改善される。

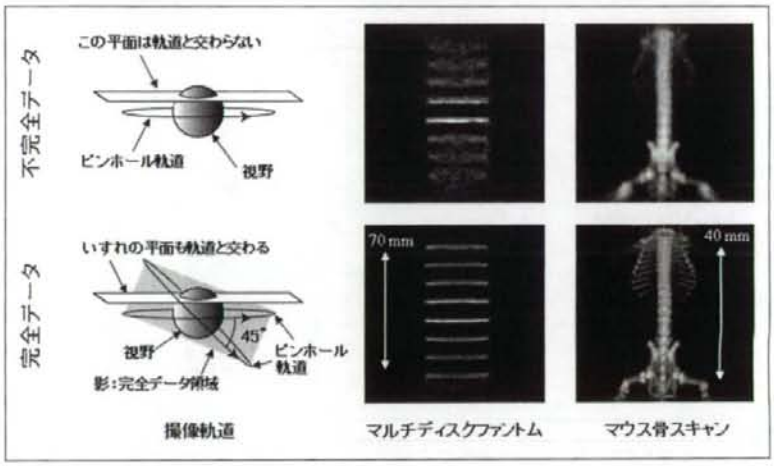

図2　従来の単一円軌道からの不完全データ（上）と開発した2軸収集軌道からの完全データ（下）による再構成画像の比較
マルチディスクファントム実験とマウス骨スキャン。従来法では画像中央断面以外は大きく歪み、完全データから再構成した画像では歪がなく、視野全体で均一な解像度が得られている。0.5mmの肋骨も鮮明に描出されている。

これに対応した3次元OSEM画像再構成法を開発した[5]。これによって、歪みのない視野全体で均一な解像度を有する3次元画像を得ることに成功した。その結果、ピンホールSPECTにおいても定量評価が可能になった。同様の試みとして、Metzlerらはヘリカル軌道によって完全データ収集し、画像歪を改善することを示した[6]。また、Beekmanらは多数のピンホールで被写体を囲むことで、検出器を静止した状態で近似的な完全データを得ている[7]。

トランケーションを許す画像再構成法

ピンホールコリメータは、撮像対象がコリメータに近いほど感度および解像度を高くできるのが特長であるが、極端に近づけるとトランケーションが生じる。その結果、再構成画像の視野の周辺で極端にカウントが高くなるアーチファクトが生じ、画像全域でもカウントが過大評価されるので、定量評価の妨げとなる。

小動物を撮像する場合は、通常、被写体が視野からはずれないように、被写体からコリメータをある程度遠ざけて撮像する。ただし、これは解像度と感度について妥協することになる。われわれは、Defriseらが2次元X線CTを対象として提案したトランケーションを許す画像再構成理論[8]を基に、これをピンホールSPECTに拡張した3次元画像再構成法TC-

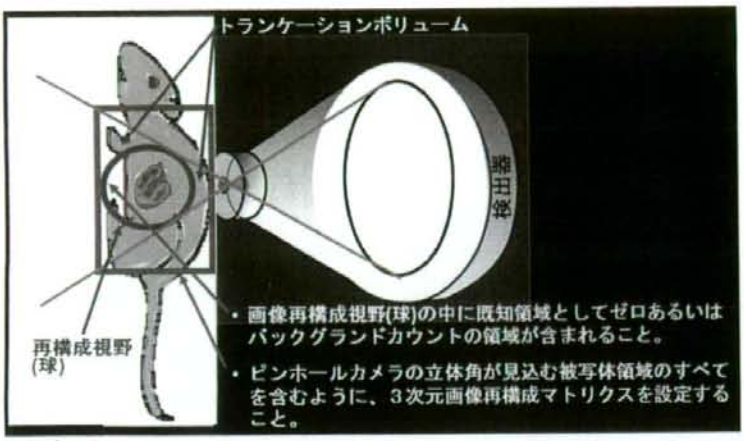

図3　ピンホールSPECTの3次元画像再構成において、トランケーションがあっても視野内は正確な画像を得るための再構成条件

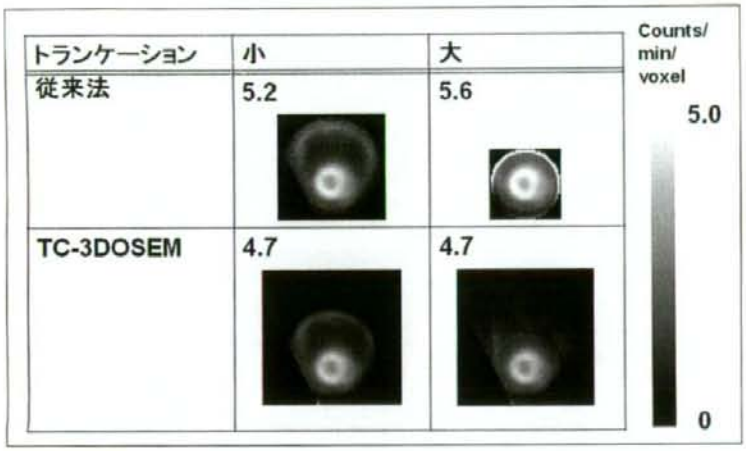

図4　TC-3DOSEMと従来法によって再構成されたラット心筋画像と心筋カウント
数値は心筋上のROIの平均カウント。実験データからトランケーション量の異なるデータを生成した。TC-3DOSEMではアーチファクトおよび過大評価が抑制され、またトランケーション量に依存しない定量画像が得られる。

3DOSEM（Truncation Compensated 3DOSEM）を開発した[9]。本画像再構成理論では、図3に示すように、①画像再構成視野（球）の中に既知領域として被写体の外側のゼロあるいはバックグランドカウントのボリュームが含まれること、および②ピンホールカメラの立体角が見込む被写体領域をすべて含むように3次元画像再構成マトリクスを設定すること、この2つの条件下において、OSEMなどの逐次近似画像再構成法によって視野内は正確な値に収束する。本手法によって、トランケーションがあっても視野内においては定量性が確保される（図4）。

小動物用SPECT装置

われわれは、ラットの心筋血流量定量などを目的とした、小型で可搬性のある小動物専用SPECT装置を開発した。装置を小型化するために導入した小型高解像度検出器は、シンチレータが臨床用SPECT装置で使用されているような平板のNaIに代えて1.5mmピッチのピクセル型NaIを使用し、光電子増倍管（Photomultiplier Tube: PMT）も、従来の3インチの大型PMTによる配列に代えて5cmのフラット位置感応型PMTで構成されている。小型高解像度検出器とピンホールコリメータの拡大撮像技術を組み合わせ[10]、コ

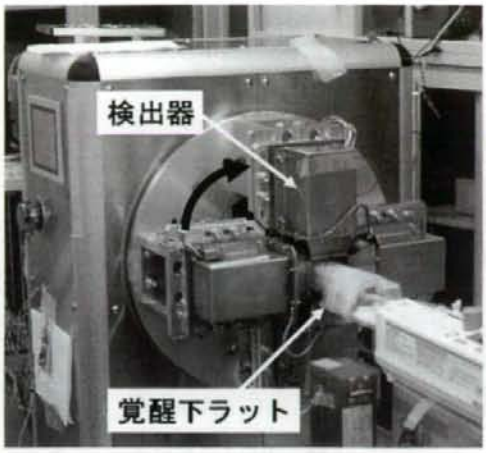

図5　われわれの開発した小動物専用マイクロSPECT装置

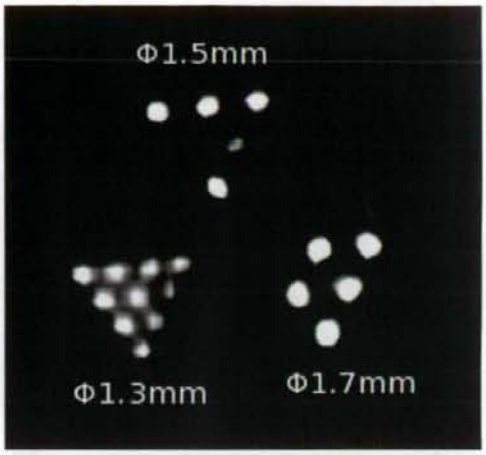

図6　マルチラインソースファントム画像
1.3mm径のラインソースが識別できている。

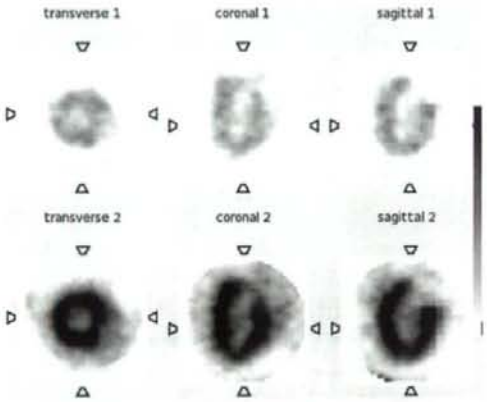

図7　本マイクロSPECT装置で得られた^{201}Tlによるラット心筋SPECT画像の1例
上：安静時、下：負荷時。安静時に対して、負荷時で血流が上昇しているのがわかる。

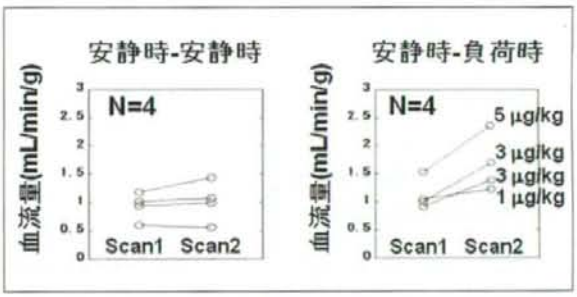

図8　本マイクロSPECT装置で得られた健常ラットの心筋血流量および血管反応性

ンパクトな小動物専用高解像度SPECT装置を開発した（図5）。ピンホールコリメータの欠点でもある低感度を補うことと高感度化のため、被写体の周囲に4台の検出器が90°間隔で配列されている。また、小動物ベッドが水平方向に回転可能となっており、異なる回転軸による撮像軌道で完全データ収集が可能である。

マルチラインソースファントム実験では、1.3mm径のラインが識別可能であった（図6）。また、本装置を用いて、覚醒下で健常ラットの心筋血流量および血管反応性を評価した。^{201}Tlを2回投与して、安静時と安静時、および安静時と血管拡張剤による負荷時の血流量を測定した。図7は本実験で得られたラット心筋SPECT画像であるが、非常に鮮明である。一連の時系列画像を動態解析して血流値が計算され、安静時と安静時では血流値に変化はなく、安静時と負荷時では血管拡張剤の量に依存して血流上昇が確認できた。本装置および画像再構成法によって得られた画像から、ラット心筋血流定量が可能であることが示された（図8）。

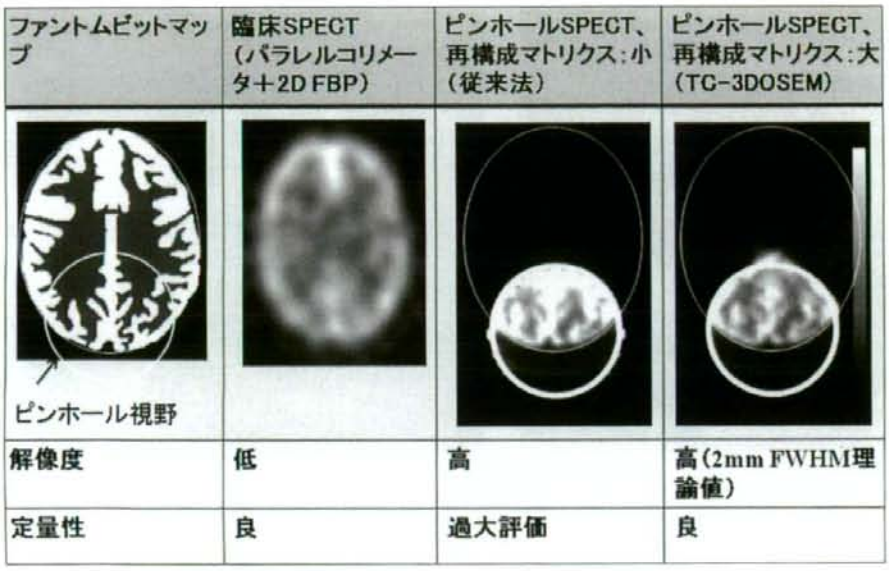

図9　脳ファントムの再構成画像
臨床SPECTでは低解像度で詳細構造は見えない。ピンホールSPECTの局所高解像度撮像では、TC-3DOSEMによる再構成画像にて、従来法で存在していたアーチファクトや過大評価がなく、詳細構造が明瞭に描出されている。

ピンホールSPECTによるヒト局所高解像度撮像

従来、ピンホールSPECTのような小視野検出器でヒトのように大きな被写体を撮像した場合、トランケーションは避けられず、それによるアーチファクトや過大評価により、定量評価は困難であった。トランケーションを許す画像再構成法を利用することで、小動物SPECTで確立したピンホールSPECTによる高解像度撮像技術が、ヒトのように大きな被写体であっても利用でき、局所小領域を拡大した高解像度定量SPECTイメージングが、トランケーションの影響なく可能となる。

ピンホールSPECTによるヒト脳局所高解像度定量撮像の可能性を評価するための物理ファントム実験を行った。ピンホールコリメータを取りつけた臨床用SPECTカメラを固定し、Hoffmanの脳ファントムを回転ステージ上で180°回転させて視野内にファントム外側の領域が含まれるように投影データを収集した。再構成マトリクスが小さい従来法と再構成マトリクスを大きくしたTC-3DOSEMで画像再構成した。また、一般の臨床用SPECTと解像度を比較するため、同じファントムをパラレルホールコリメータでデータ収集し、2D FBP法で画像再構成した。図9に示すように、臨床SPECTでは低解像度で詳細構造は見えなかった。また、ピンホールSPECTデータを従来法で再構成した場合はアーチファクトが見られ、視野全域でカウントが過大評価されていた。一方、ピンホールSPECTデータをTC-3DOSEMで再構成した場合、アーチファクトも過大評価もなく、高解像度で詳細構造が確認できた。

本撮像技術によって、微小腫瘍検出、血管プラークイメージング、てんかん焦点同定、部分容積効果のない血流定量などが可能になると考えられる。実際に、われわれは図10のような局所高解像度定量SPECT装置を開発中で、脳全域画像と局所高解像度画像を提供する。

おわりに

従来、研究の域を脱しなかったピンホールSPECTは、新しい撮像技術や画像再構成法の開発によって、高解像度かつ定量評価可能な小動物用SPECTとして実用化の域に達した。また、トランケーションを許

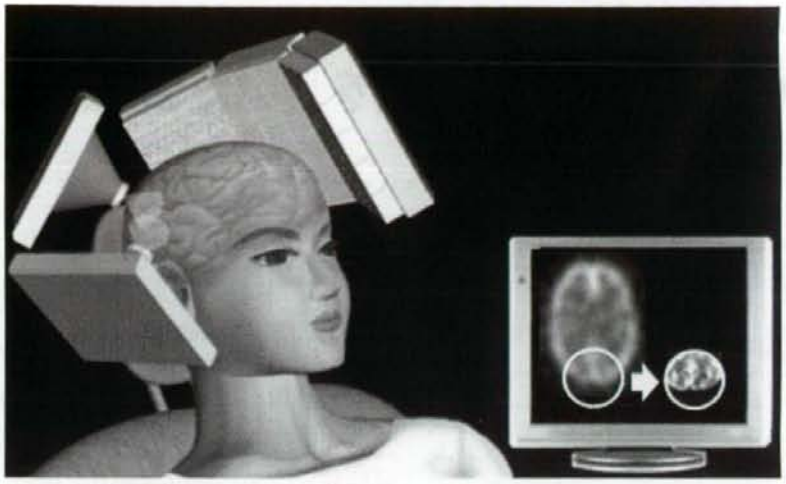

図10　頭部局所高解像度SPECT装置のイメージ図

す画像再構成法によって、ピンホールSPECTを利用したヒトの局所高解像度定量SPECTが開発されようとしている。これまで、解像度が低いといわれてきたSPECT撮像において、新しい撮像技術や画像再構成法などの開発によって高解像度定量撮像が可能になりつつある。

参考文献

1) Meikle SR et al: Small animal SPECT and its place in the matrix of molecular imaging technologies. Phys Med Biol 50(22): R45-61, 2005
2) 間賀田泰寛: 各社製品の性能比較. PET journal (2): 27-29, 2008
3) Vanhove C et al: Interest of the ordered subsets expectation maximization (OS-EM) algorithm in pinhole single-photon emission tomography reconstruction: a phantom study. Eur J Nucl Med 27(2): 140-146, 2000
4) Tuy HK: An inversion formula for cone-beam reconstruction. SIAM J Appl Math 43(3): 546-552, 1982
5) Zeniya T et al: A new reconstruction strategy for image improvement in pinhole SPECT. Eur J Nucl Med Mol Imaging 31(8): 1166-1172, 2004
6) Metzler SD et al: Helical pinhole SPECT for small-animal imaging: a method for addressing sampling completeness. IEEE Trans Nucl Sci 50(5): 1575-1583, 2003
7) Beekman FJ et al: U-SPECT-I: a novel system for submillimeter-resolution tomography with radiolabelled molecules in mice. J Nucl Med 46(7): 1194-1200, 2005
8) Defrise M et al: Truncated Hilbert transform and image reconstruction from limited tomographic data. Inverse Probl 22(3): 1037-1053, 2006
9) Zeniya T et al: 3D-OSEM reconstruction from truncated data in pinhole SPECT. Nuclear Science Symposium Conference Record, 2007. NSS'07, IEEE, 4205-4207
10) Zeniya T et al: Use of a compact pixellated gamma camera for small animal pinhole SPECT imaging. Ann Nucl Med 20(6): 409-416, 2006

Clinical Usability of a Compact High Resolution Detector for High Resolution and Quantitative SPECT Imaging in a Selected Small ROI

Tsutomu Zeniya, Hiroshi Watabe, *Member, IEEE*, Hiroyuki Kudo, *Member, IEEE*, Yoshiyuki Hirano, Kotaro Minato, *Member, IEEE*, and Hidehiro Iida, *Member, IEEE*

***Abstract*– SPECT using compact high resolution detector or pinhole collimator allows to image physiological functions with high spatial resolution. However, when field-of-view (FOV) is smaller than the object, the projection data are truncated by radioisotope outside FOV. The truncation causes artifact and overestimation, which decreases quantitative accuracy. Recently Defrise et al proposed a new truncation-compensated reconstruction method, that is, the truncated data can be successfully reconstructed by fulfilling following conditions. First, FOV contains zero or background counts outside the object as known value. Second, reconstructed image space is large enough to contain the whole support of the object. They demonstrated their theory by 2D X-ray CT simulation. This study was aimed at evaluating clinical-SPECT usability of a reconstructed image of a selected small region-of-interest (ROI) with the above Defrise's method. This evaluation was performed by computer simulation with a numerical human brain phantom and a detector with 2-mm resolution, 48-mm FOV and a parallel collimator. The projection data were acquired including the area outside the brain. After adding Gaussian noise, the projection data were reconstructed by maximum likelihood expectation maximization (MLEM) method on the reconstruction matrix large enough to contain the whole support of the brain. This simulation showed that the truncation compensated reconstruction method could provide the image with high resolution and the counts almost equivalent to that of original image in the selected small ROI without the effect of truncation for human brain. In conclusion, this result suggests that a compact high resolution detector can be used for quantitatively reconstructing a selected small ROI with clinical SPECT camera. This technique can also use the pinhole collimator instead of the compact high resolution detector.**

I. Introduction

SPECT using compact high resolution detector or pinhole collimator allows to image physiological functions with high spatial resolution [1]. However, when such a small field-of-view (FOV) detector is applied for a large object like human, the projection data are truncated by radioisotope outside the FOV. The truncation causes artifact and overestimation, which quantitative accuracy. Recently Defrise et al proposed a new truncation-compensated reconstruction method [2]. They demonstrated their theory by 2D X-ray CT simulation. The aim of this study was to evaluate clinical-SPECT usability of a reconstructed image of a selected small region-of-interest (ROI) with the above Defrise's method. This evaluation was performed by 2D computer simulation with a numerical human brain phantom.

II. Materials and Methods

A. Defrise's truncation-compensated reconstruction theory

Defrise's theory compensates the artifact and overestimation due to truncation and exactly reconstructs for FOV, by fulfilling the conditions as shown in Fig. 1. Projection data must be acquired under first condition. And then, the projection data must be reconstructed by iterative reconstruction method such as maximum likelihood expectation maximization (MLEM) method [3] under second condition.

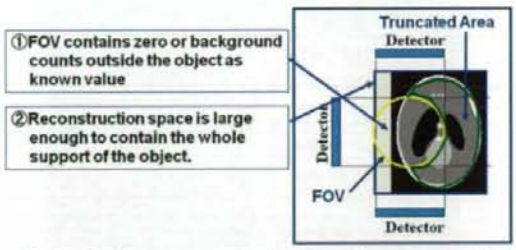

Fig. 1. Conditions to compensated artifact and overestimation due to truncation in Defrise's theory.

B. Computer Simulation

Figure 2 shows the numerical human brain phantom used in this simulation. Image matrix is 90 pixel × 110 pixel. Assuming pixel size of 2 mm, the image size is 180 mm × 220 mm. Pixel values are 1 or 0.

A compact high resolution detector is with 2-mm resolution, 48-mm FOV, 24 bins and a parallel-hole collimator. Projection data for ROI shown by red circle in Fig. 2 were acquired by a circular orbit shown by green line, over 180°,

Manuscript received November 14, 2008. This work was supported in part by the Grant-in-Aid for Scientific Research (B) of the Ministry of Education, Culture, Sports and Technology (20500435), Japan, and the Grant for Translational Research from the Ministry of Health, Labour and Welfare (MHLW), Japan.

T. Zeniya, H. Watabe, Y. Hirano and H. Iida are with the Department of Investigative Radiology, Advanced Medical Engineering Center, National Cardiovascular Center Research Institute, 5-7-1 Fujishirodai, Suita, Osaka 565-8565 Japan (e-mail: zeniya @ri.ncvc.go.jp).

T. Zeniya and K. Minato are with the Graduate School of Information Science, Nara Institute of Science and Technology, Japan.

H. Kudo is with the Department of Computer Science, Graduate School of Systems and Information Engineering, University of Tsukuba, Japan.

with 3°step and 60 views. This ROI included the area outside the brain. After adding Gaussian noise, the projection data reconstructed by MLEM method, on the reconstruction matrix of 90 pixel × 110 pixel large enough to contain the whole support of the brain to satisfy the condition of Defrise's theory. To compare with conventional reconstruction method using small reconstruction matrix, projection data with 24 bin were also reconstructed on the reconstruction matrix of 24 pixel × 24 pixel. The number of iteration in MLEM reconstruction was 24 for each method.

To compare with conventional clinical SPECT, untruncated projection data including the whole of the brain were acquired by a 220-mm large FOV (22 bin) detector with low resolution of 10 mm, over 360°, with 3° step and 120 views. After adding Gaussian noise, the projection data were reconstructed by ordered subsets expectation maximization (OSEM) method [4] which is an accelerated MLEM. The OSEM parameters were 8 subsets and 3 iterations.

As reference image, untruncated projection data including the whole of the brain were acquired by a 220-mm large FOV (110 bin) detector with high resolution of 2 mm, over 360°, with 3° step and 120 views. After adding Gaussian noise, the projection data were reconstructed by OSEM method with 8 subsets and 3 iterations. However, this detector is impractical because it is too expensive if manufactured.

The images obtained in this simulation were visually compared, and also the profiles of the images were obtained on line shown by yellow in Fig. 2 to compare quantitatively.

In this simulation, the effects of attenuation, scatter and blurring by collimator were not considered because this simulation was aimed at evaluating truncation-compensated method.

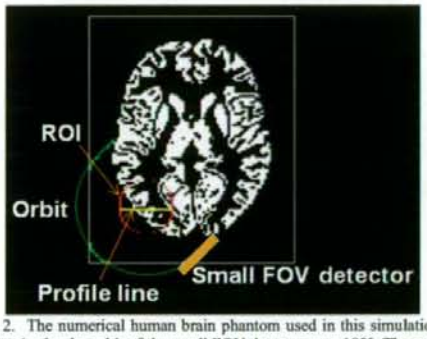

Fig. 2. The numerical human brain phantom used in this simulation. The green line is circular orbit of the small FOV detector over 180°. The red circle is ROI. The yellow line is the position of profiles shown Fig. 4. Pixel values are 1 or 0.

III. Results and Discussion

Figure 3(a) shows the image reconstructed from untruncated projection data using the small FOV detector with low resolution. The obtained image had low resolution. The detail of brain structure was not observed.

Figure 3(b) shows the image reconstructed from untruncated projection data using the large FOV detector with high resolution. The image with high resolution was obtained and the fine structure was observed. However, such a high resolution and large FOV detector is impractical because it is too expensive if manufactured.

Figure 3(c) shows the image reconstructed from truncated projection data obtained using the small FOV detector with high resolution. The projection data were reconstructed on the small reconstruction matrix as conventional reconstruction method. The reconstructed image had artifact and the pixel counts were significantly overestimated.

Figure 3(d) shows the image reconstructed from truncated projection data using the small FOV detector with high resolution. The projection data were reconstructed on the large reconstruction matrix as proposed reconstruction method. The obtained image was with high resolution and the pixel counts almost equivalent to that of original image without the effect of truncation in the selected small ROI.

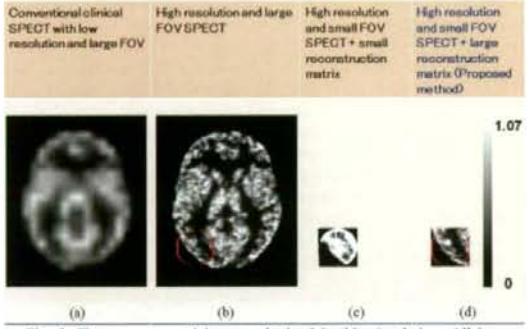

Fig. 3. The reconstructed images obtained in this simulation. All images were displayed with the range of same gray scale [0-1.07] (a) The image obtained from the untruncated projection data of large FOV detector with low resolution as conventional clinical SPECT. (b) The image obtained from the untruncated projection data of large FOV detector with high resolution as the reference image. (c) The image reconstructed from the truncated projection data of small FOV detector with high resolution, on the small reconstruction matrix as conventional reconstruction method. (d) The image reconstructed from the truncated projection data of small FOV detector with high resolution, by the large reconstruction matrix as proposed reconstruction method.

Figure 4 shows the line profiles in a small ROI on the images obtained from the high-resolution detectors. When the truncated projection data from small FOV detector were reconstructed on the small reconstruction matrix, the obtained image had extremely high counts on the edge of and the pixel counts were wholly overestimated. On the other hand, when the truncated projection data from small FOV detector were reconstructed on the large reconstruction matrix, the profile of the image had good agreement with that of the image from the untruncated projection data.

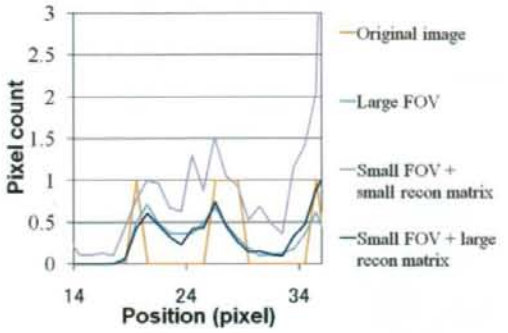

Fig. 4. In a small ROI, the line profiles on the image obtained by reconstructing data from high-resolution detector by each method.

IV. Conclusion

These results suggest that a compact high resolution detector can be used for quantitatively reconstructing a selected small ROI with clinical SPECT camera. This technique can also use the pinhole collimator instead of the compact high resolution detector.

References

[1] S. R. Meikle, P. Kench, M. Kassiou, and R. B. Banati, "Small animal SPECT and its place in the matrix of molecular imaging technologies," *Phys. Med. Biol.*, vol. 50, no. 22, pp. R45-R61, 2005.

[2] M. Defrise, F. Noo, R. Clackdoyle, and H. Kudo, "Truncated Hilbert transform and image reconstruction from limited tomographic data," *Inverse Problems*, vol. 22, no. 3, pp. 1037-1053, 2006.

[3] L. A. Shepp and Y. Vardi, "Maximum likelihood reconstruction for emission tomography," *IEEE Trans. Med. Imaging*, vol. 1, no. 2, pp. 113-122, 1982.

[4] H. M. Hudson and R. S. Larkin, "Accelerated image reconstruction using ordered subsets of projection data," *IEEE Trans. Med. Imaging*, vol. 13, no. 4, pp. 601-609, 1994.

Combination of a High Resolution Detector with Small FOV and a Low Resolution Detector with Large FOV for High Resolution and Quantitative SPECT

Tsutomu Zeniya, Hiroshi Watabe, *Member, IEEE*, Hiroyuki Kudo, *Member, IEEE*, Yoshiyuki Hirano, Kotaro Minato, *Member, IEEE*, and Hidehiro Iida, *Member, IEEE*

Abstract– **SPECT using compact high resolution detector or pinhole collimator allows to image physiological functions with high resolution. However, when region-of-interest (ROI) is smaller than the object, the projection data are truncated due to radioisotope outside ROI. The truncation causes artifact and overestimation, which decrease quantitative accuracy. In theory, to eliminate the artifact and the overestimation due to truncation, the untruncated data from another large field-of-view (FOV) detector can be used even if the detector has low resolution. This study was aimed at evaluating feasibility of combination of a small FOV high resolution detector and a large FOV low resolution detector in clinical circumstance. This evaluation was performed by computer simulation with a numerical torso phantom. We tested whether the image in a selected small ROI (in this case, ROI was heart) can be obtained with high resolution and without artifact and overestimation. The small FOV detector with high resolution was with 1.14-mm resolution, 80-mm FOV and parallel collimator. The whole of heart was included in this FOV, but the surrounding area was truncated. The large FOV detector with low resolution has 9-mm resolution, 360-mm FOV and parallel collimator like conventional clinical SPECT. The untruncated projections including the whole of thorax were acquired by this detector. Gaussian noises were added to all projection data. Data from the small detector were reconstructed by maximum likelihood expectation maximization (MLEM) as iterative method, on the reconstruction matrix large enough to contain the whole of thorax. The reconstructed image from the large FOV detector was used as an initial image in iterative reconstruction. The image obtained by our proposed method had high resolution and the counts almost equivalent to that of original image in the small ROI. In conclusion, this result suggests feasibility of the combination of two detectors with small and large FOV to quantitatively obtain high-resolution image of a selected small ROI with clinical SPECT.**

Manuscript received November 14, 2008. This work was supported in part by the Grant-in-Aid for Scientific Research (B) of the Ministry of Education, Culture, Sports and Technology (20500435), Japan, and the Grant for Translational Research from the Ministry of Health, Labour and Welfare (MHLW), Japan.

T. Zeniya, H. Watabe, Y. Hirano and H. Iida are with the Department of Investigative Radiology, Advanced Medical Engineering Center, National Cardiovascular Center Research Institute, 5-7-1 Fujishirodai, Suita, Osaka 565-8565 Japan (e-mail: zeniya @ri.ncvc.go.jp).

T. Zeniya and K. Minato are with the Graduate School of Information Science, Nara Institute of Science and Technology, Japan.

H. Kudo is with the Department of Computer Science, Graduate School of Systems and Information Engineering, University of Tsukuba, Japan.

I. Introduction

SPECT using compact high resolution detector or pinhole collimator allows to image physiological functions with high spatial resolution [1]. However, when such a small field-of-view (FOV) detector is applied for a large object like human, the projection data are truncated by radioisotope outside region-of-interest (ROI). The truncation causes artifact and overestimation, which quantitative accuracy. Truncation-compensated reconstruction theory proposed by Defrise et al uses area outside the object with ROI as a prior knowledge to solve the truncation problem [2]. Defrise's theory can't be applied for the case that ROI does not contain the area outside the object. The aim of this study was to evaluate feasibility fo combination of a small-FOV high-resolution detector and a large-FOV low-resolution detector in clinical circumstance. We tested whether the image in a selected small ROI (in this case, ROI was heart) can be reconstructed with high resolution and without the effect of truncation by using untruncated data from the large FOV detector, which do not need to have high resolution, even if ROI in small FOV detector with high resolution does not contain the area outside the object. This evaluation was performed by 2D computer simulation with a numerical human torso phantom.

II. Materials and Methods

A. Support from large-FOV low-resolution detector for truncation problem

As shown in Fig. 1, our proposed method uses untruncated data from the large FOV detector with low resolution, in order to compensate the artifact and overestimation due to truncation in small FOV detector.

Our proposed approach based on iterative reconstruction method such as maximum likelihood expectation-maximization (MLEM) [3] or ordered-subsets expectation-maximization (OSEM) [4] algorithm is, as follows:

Step1: the object is reconstructed using OSEM from untruncated data of the large FOV detector with high resolution;

Step2: In the MLEM reconstruction, the image reconstructed from the large FOV detector is used as initial

978-1-4244-2715-4/08/$25.00 ©2008 IEEE